



The variable radial depth of cut in finishing machining of thin-walled blade based on the stable-state deformation field

Yaohua Hou^{1,2} · Dinghua Zhang^{1,2} · Ying Zhang^{1,2} · Baohai Wu^{1,2}

Received: 5 August 2020 / Accepted: 7 December 2020 / Published online: 21 January 2021
© The Author(s), under exclusive licence to Springer-Verlag London Ltd. part of Springer Nature 2021

Abstract

Due to the low stiffness of the thin-walled part, the larger deformation error occurs in the milling process, and the machining precision and quality cannot be satisfied. Previous studies of the tool path generation methods for the deformation error control mainly focused on the deformation calculation of the cutting block and lacked how to control the machining deformation of the complex free-form surface of the thin-walled blade by the generated tool path. This paper firstly establishes the elastic deformation error model of the thin-walled part milling process depending on the stiffness matrix of the workpiece before the cutting process. Furthermore, the cutting force model in ball-end milling and the stable-state deformation field are studied to calculate the cutting contact points sequence with less machining deformation error for the tool path planning process. The radial depth of cut of the generated tool path is optimized with different strategies to calculate the suitable cutting contact points for deformation control of the thin-walled part milling process by applying the relationship between the cutting parameters and elastic deformation. Finally, thin-walled blades are machined with four different cutting paths. The measured results demonstrate that the optimized tool paths are effective for deformation error control of the thin-walled blades milling process considering the machining precision and efficiency.

Keywords Thin-walled blade · Deformation control · Cutting sequence · Variable depth of cut

1 Introduction

The thin-walled parts with the characters of higher strength, higher durability and less weight are widely utilized in the aviation industry where it requires a mass of lightweight parts [1]. However, due to the low stiffness of the thin-walled parts, the elastic deformation caused by the cutting force in the milling process cannot be avoided, resulting in the unacceptable machining precision. Especially in the aero-engine field, the machining accuracy of the thin-walled blade directly affects the engine performance [2]. Therefore, how to manufacture

the high-quality blade is still a challenging problem in the aviation industry field [3].

At present, the researches of the machining error control for the thin-walled parts can be categorized as machine tool structure design, fixture design, cutting conditions optimization and cutting path generation [4]. The effectiveness of the machine tool structure [5] and fixture designs [6, 7] has been proved in previous studies. However, the extra hardware cost is increased due to the improvement of productivity in these methods. For mass machining, the improvements of the manufacture process (include cutting conditions optimization and cutting path generation) are the primary choice to achieve high machining precision and decrease the hardware cost, effectively.

The cutting condition optimization strategy is widely studied in the current researches. In thin-walled parts machining process, the cutting force determined by variable cutting parameters is the main factor causing the elastic deformation of the workpiece. Therefore, the cutting force and the cutting contact (CC) area modelling attract the most attentions of the researchers and are developed to predict the real cutting force and elastic deformation in the milling process, precisely. After that, the cutting parameters are recalculated or the real CC

✉ Ying Zhang
zhangyingcdim@nwpu.edu.cn

¹ Key Laboratory of High Performance Manufacturing for Aero Engine (Northwestern Polytechnical University), Ministry of Industry and Information Technology, Xi'an 710072, China

² Engineering Research Center of Advanced Manufacturing Technology for Aero Engine (Northwestern Polytechnical University), Ministry of Education, Xi'an 710072, China

points are compensated to ensure that the actual material removal is as much as close to the nominal cutting allowance to satisfy the machining precision. Ratchev et al. [8] modelled the cutting force for the thin-walled part milling process. Unlike the classic modelling process [9], the decreased depth of cut caused by the deformation of the part was considered. With the flexible cutting force model, the complex milling process of the thin-walled part was described. Different cutting states of the cutting elements were classified by the finite element (FE) analysis [10]. Finally, the cutting force and the elastic deformation were predicted in the cutting process simulation, and the deformation error could be compensated with mirror method by adjusting the nominal CC points in the real milling process [11]. Similarly, Wan et al. [12] introduced the cutting force model, the relationship between cutting tool and part and the variation of the part stiffness to predict the static error in the milling process applying the FE method with irregular grids. Kang and Wang [13] proposed different iteration methods in the compensation process with the FE method to improve the efficiency and accuracy of the prediction model.

Based on the cutting force model and the FE method, the deformation prediction and the error compensation with the mirror algorithm for CC points are effective to improve the machining precision for thin-walled part milling process. However, the iteration process of the machining and measuring procedures based on the machining error compensation method with the dimension data is more convenient in the practical workshop [14]. Brandy et al. [15] proposed the process-intermittent inspection technology previously in the thin-walled part machining process. The machining error was measured in the semi-finish process by the on-machine measurement (OMM) for compensation calculation to control the nominal tool path in the finish process and improve the machining precision. Guissa et al. [16] applied the process-intermittent probe in the thin-walled part machining process to obtain the machining error in each layer. Applying the relationship between the elastic deformation and the depth of cut, the compliance coefficient was fitted and then presented to predict the nominal depth of cut in the next layer of the machining process. The new nominal depth of cut was proved to be effective to improve the machining precision. Cho et al. [17] developed the machining error compensation system with the OMM. The error zone and deflection after machining were introduced to describe the error distribution, and the tool path was regenerated with the compensation method, resulting in a higher machining accuracy. Similarly, the error compensation and geometry modelling algorithm with the OMM data were applied to the thin-walled blade milling process with satisfactory precision [18].

The above researches of the cutting force and the deformation prediction and the machining error measurement can be summarized as the compensation process of the nominal CC points or the designed depth of cut with the machining

deformation [19]. However, the application of the error compensation algorithm may cause the overcut situation for the increment of the cutting depth. The suitable choice of the cutting parameters is required to ensure the reliability of the compensation algorithm. Besides, if the compensated machining error cannot satisfy the precision, another compensation process is required, which is time-consuming. Therefore, the direct error control methods are needed.

Considering that the cutting force is determined by the cutting parameters, the new tool path is generated by decreasing the axial and the radial depths of cut expected to reduce the cutting force and the deformation [20]. However, the material removal rate will be lower if the depth of cut is decreased blindly, which leads to the long-term machining procedure and reduces the efficiency of the cutting process. Especially, the constant allowance method is widely proposed when planning the cutting path. The smaller allowance is necessary to reduce the cutting force and the deformation in the finish milling process since the stiffness of the part is much lower than the original stock. To solve the inefficiency of the machining process caused by the small depth of cut, Yan et al. [21] introduced a new tool path planning method with various depths of cut considering the constraints of the elastic deformation in the thin-walled part machining process. The constraint of the maximum deformation value from the machining tolerance was implemented to calculate the machining allowances of each layer from the stock to the final shape based on the stiffness of the final part. The blade machining instance validated that the deformation error satisfied the machining tolerance and the various depths of cut planning method was effective. Nevertheless, only the axial depth of cut for the allowance design in each cutting layer was concerned. The parallel cutting path distributed from the free end to the fixed end was still the main path planning method for the thin-walled cantilever part machining process. The calculation of the radial depth of cut in the cutting layer including CC points was ignored. Besides, the stiffness variation prediction of each layer during the machining process was inaccuracy.

At present, iso-parametric, iso-planar and constant scallop height methods are widely applied in the machining process of the free-form surface [22]. Chiou et al. [23] developed the multi-axis machining potential field aiming to maximum the machining strip width. The free-form surface was divided into different regions to guarantee that the strip width located in each region was maximum to guarantee the machining efficiency. Hu et al. [24] employed the machining potential field with the optimized feed rate to plan the tool path and the efficiency was improved. However, these effective tool path planning methods solved the machining error and efficiency problems from the geometry. The stiffness variation and the elastic deformation during the practical machining process of the thin-walled part were not considered in these researches. Only a few researches focused on this problem. Wang et al. [4]

proposed the material removal algorithm by cutting the minimum displacement of the cutting block firstly. Although the total deformation of the whole part is smaller, the positions of the cutting blocks were not continuous in the machining process. As a result, the engage and the retract movements in the finish milling process caused significant “bump” in the surface profile leading to an unacceptable machining quality. Also, the efficiency was decreased due to the frequent engage and retract movements. Therefore, Koike et al. [25] proposed the continuous material removal sequence by cutting the low stiffness block preferentially. Although the disadvantage of the former algorithm was fixed, the new algorithm was limited to the thin-walled plate machining. The cutting sequence optimization strategy of the thin-walled free-form surface machining process was still lacked.

With the above researches of the tool path planning, the elastic deformation of the thin-walled part machining could be limited in an acceptable threshold. However, most researches focused on the deformation calculation and the cutting sequence of the allowance block. The elastic deformation of different regions influenced by the variation of the surface stiffness during the thin-walled part machining process was not considered. Eventually, the cutting path is planned by the experience; the general cutting path generation framework for the thin-walled part milling process based on the variation of the workpiece stiffness was not established. To overcome these disadvantages, this paper proposed cutting path generation algorithm for the thin-walled part milling process based on the stable-state deformation field. Firstly, the static deformation field of the machining surface is established by the stiffness matrix. Then, the cutting directions with the minimum variation of the part stiffness during milling process are calculated with the proposed theory, that is, the stable-state deformation field. Furthermore, the machining deformation error model of the thin-walled part is developed with the cutting force model in ball-end milling. With all these preparations, the optimization algorithm for the radial depth of cut is developed to reduce the machining deformation error. Finally, different cutting paths are implemented to machine the thin-walled blades in a three-axis machine tool to validate the effectiveness of the proposed algorithm.

2 The framework of the methodology

During the CNC machining process of the thin-walled part, the cutting force could cause the severe elastic deformation due to the low stiffness of the workpiece. In detail, the deformation is expressed as the unexpected location of the CC points, which means the real CC points are not in the nominal positions. As a result, the dimension errors of the workpiece cannot satisfy the design accuracy. The displacement of each point of the part is expressed as

$$K^G \delta = F \quad (1)$$

where K^G is the stiffness matrix of the whole part, δ is the displacement vector of all points and F is the cutting force acting on the part.

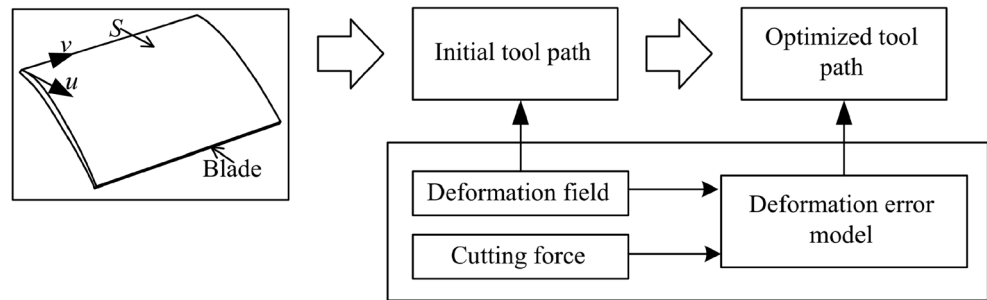
According to the above formula, it is obvious that the cutting force and the workpiece stiffness are the key factors in the deformation control issues of the thin-walled part milling process. As mentioned in the previous section, a lot of researches on the cutting force prediction and control have been developed. Similarly, a large number of machining error compensation algorithms have been developed to reduce the machining errors that still exist after processing. However, as the ability of resisting elastic deformation of the materials or structures under the stress, the stiffness of the thin-walled part plays a key role in the machining process, and only a few studies have been focused, which will be discussed in this paper. At present, the acquisitions of the workpiece stiffness are concentrated on the real measurement and the FE calculation [21]. Since the stiffness measurement process can only be performed after the workpiece machining, various processing methods are required to guarantee the precise shape of the workpiece in order to ensure the accuracy of the measuring results. Nevertheless, the measurement process of the stiffness is time-consuming. In this case, the FE calculation is still the general method introduced in this paper to determine the stiffness matrix. Due to the differences between the boundary condition and the real milling process, there are deviations from the final results of the stiffness. However, the calculation of the stiffness could be carried out before machining, which still owns the high practical value.

Therefore, the paper firstly establishes the deformation field and the cutting force model in ball-end milling. Combined with the simulation of the part deformation, the approximate cutting path directions that lead to the minimum deformation of the overall workpiece are generated. Finally, a novel deformation calculation algorithm is developed to optimize the radial depth of cut to obtain the new cutting path which can be applied in milling the thin-walled part with less machining errors. Series machining experiments will be executed to verify the effectiveness and efficiency of the cutting path planning and the radial depth of cut optimization, as shown in Fig. 1.

3 The initial tool path planning based on the stable-state deformation field

For machining process, planning a reasonable cutting path is the primary factor to ensure the machining accuracy of the product, where it includes the cutting tool shape, the CC point position and the tool axis orientation. In addition, the interference problem between the cutting object and the non-cutting object needs to be solved in cutting path planning. After

Fig. 1 The framework of the methodology



meeting the above requirements, it is still necessary to satisfy the machining precision and improve the machining efficiency. For thin-walled milling process, the deformation error control of the workpiece should be paid attention primarily in the tool path planning.

During the thin-walled part machining process, the properties such as the stiffness of the remaining workpiece cannot stay constant as the material is removed continuously since for the dynamic variation of the milling process. Moreover, with the different material removal sequences, the stiffness of the same position in the remaining workpiece will be different. In addition, the larger stiffness region of the workpiece can support the cutting process in the low stiffness region. Therefore, in order to control the deformation error of the thin-walled part machining process, it is necessary to remove the material of the low stiffness region preferentially and ensure that the stiffness of the specified position of the remaining workpiece maintains constant before the cutter has reached. According to the above description, the following definition is given:

In the milling process, the stiffness of the uncut area of the workpiece varies as the material is removing. With different cutting path planning strategies, the variations of the uncut area stiffness are different. The cutting sequence leading to the minimum variation of the stiffness is regarded as the stable-state cutting sequence, and the deformation field of this milling process is the stable-state deformation field.

To achieve such requirements, it is necessary to determine the precise deformation of the workpiece by the detail application of Eq. (1). The three components, the stiffness, the cutting force and the deformation error model, are presented in the following sections.

3.1 The establishment of the deformation field for thin-walled part

3.1.1 The establishment of the global stiffness matrix

To establish the stiffness matrix, the entire workpiece (as shown in Fig. 2) is firstly divided into a series of elements $E_r (r = 1, 2, \dots, n_E)$ and nodes $N_i (i = 1, 2, \dots, n)$ with a given number according to the specified grid size by the FE method, where the subscripts of the elements and the nodes represent

their orders, and each node corresponds to its own coordinate (x, y, z) . According to the attributes of the element, each element contains a certain number of nodes, and the node belonging to the element E_r is marked as $N_i^{E_r}$ with the constant node number i . Taking C3D8 element from Abaqus software as an example, the hexahedral mesh has 8 nodes. With these concepts, the element stiffness matrix K^{E_r} about the element E_r is established as follows:

$$K^{E_r} = [K_{ij}]_{8 \times 8}, \quad (2)$$

where i, j are the node number, respectively; the set of values of i, j depends on the node number contained in E_r ; and K_{ij} is expressed as the force acting on the i th node when the j th node has a unit displacement and the other nodes are displaced to zero. The detail stiffness values in the x, y, z directions are expressed as the following form:

$$K_{ij} = \begin{bmatrix} K_{xx} & K_{xy} & K_{xz} \\ K_{yx} & K_{yy} & K_{yz} \\ K_{zx} & K_{zy} & K_{zz} \end{bmatrix}. \quad (3)$$

In order to obtain the global stiffness matrix, each element stiffness matrix is proposed for the assembling process that is to fill each stiffness values K_{ij} with the node number $\{i, j\}$ into the corresponding position in the global stiffness matrix. The same node number $\{i, j\}$ in different element stiffness matrix K^{E_r} should be added to confirm the stiffness value in the global stiffness matrix K^G that is expressed as:

$$K^G = \sum_r T_K^T K^{E_r} T_K, \quad (4)$$

where T_K is the transformation matrix and is applied to extend the element stiffness matrix to the global stiffness matrix according to the same node number. The coordinate transformation function should be integrated in T_K if the element stiffness matrix and the global stiffness matrix are in the different coordinate systems.

Since the global stiffness matrix K^G is singular without setting boundary condition after the assembling process, it cannot be fed into Eq. (1) to calculate the applied force or deformation. In this case, the boundary constraint is presented

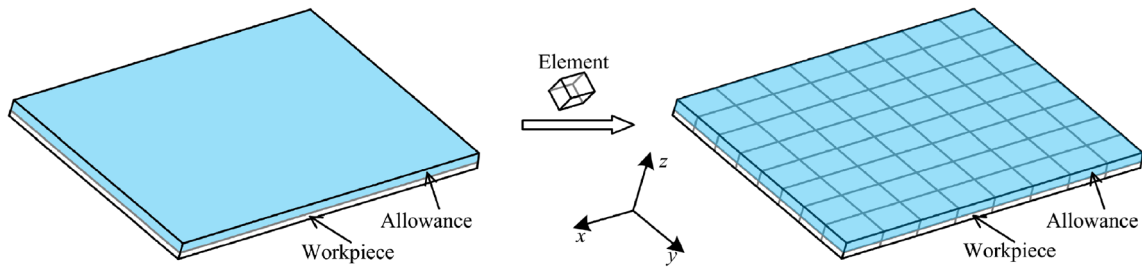


Fig. 2 The dividing process of the workpiece with FE method

to solve such problem. Taking the thin-walled blade (see the blade model in Fig. 3) as an example, one end is clamped. Therefore, the nodes in the fixed area will not displace no matter how large the cutting force is applied according to the definition of K_{ij} . To achieve such setting, the large number is applied in these nodes to ensure the success of the FE operation.

3.1.2 The establishment of the global deformation field

After the above processes, the global stiffness matrix of the workpiece can be presented to calculate the overall deformation under a certain force. However, this operation can only obtain the overall displacements of the workpiece when it is stressed at a definite force, and the deformation of the specific position of the workpiece cannot be determined. Therefore, it is necessary to establish a stiffness field of the machining surface of the workpiece to describe the deformation trend of a specific position during the material removal process. Since the stiffness of the fixed nodes approach infinity, it is inconvenient to describe the workpiece deformation by the concept of the stiffness. Considering that the trend of the stiffness field is opposite to the variation of the workpiece deformation in the same conditions, the deformation field (known as the compliance field) constructed by the node deformations under the unit force is proposed to describe the trend of the stiffness field and is developed to describe the deformation of the machining surface under the cutting force.

Different from the experimental method presented in [21] that measures the stiffness field directly, the paper proposes a

calculation method of the workpiece surface S based on the stiffness matrix. Equation (1) is expanded as follows:

$$\begin{bmatrix} K_{11} & \cdots & K_{1n} \\ \vdots & \ddots & \vdots \\ K_{n1} & \cdots & K_{nn} \end{bmatrix} \begin{bmatrix} \delta_1 \\ \vdots \\ \delta_n \end{bmatrix} = \begin{bmatrix} F_1 \\ \vdots \\ F_n \end{bmatrix}, \tag{5}$$

where n is the total number of nodes; the element in K_{ij} ($i, j = 1, 2, \dots, n$) is shown in Eq. (3); and δ_i and F_i contain three components that are directions x, y, z , respectively. In this formula, only the displacement $\delta = (\delta_1, \delta_2, \dots, \delta_n)^T$ of each node of the workpiece under a set of forces $F = (F_1, F_2, \dots, F_n)^T$ is described.

To acquire the deformation field, the unit force is performed to the specific position to calculate the displacements of the corresponding point sampled from the workpiece surface with a certain precision. Then, the deflection of the displacement is interpolated to establish the deformation field according to the position of the discrete point. Due to the existence of the FE mesh, the nodes in the workpiece surface can be directly used as the discrete points. The following performance is presented to extract the node set S_P of the discrete points belonging to the surface, that is:

$$S_P = \{P | dist(P(N_i), S) < \Delta\}, \tag{6}$$

where function $dist$ is used to calculate the distance between two parameters, P represents the discrete point of N_i , S is the surface of the workpiece (see Fig. 3) and Δ is the minimum size of the element in the meshing process. The node satisfying the above formula is the point belonging to the workpiece

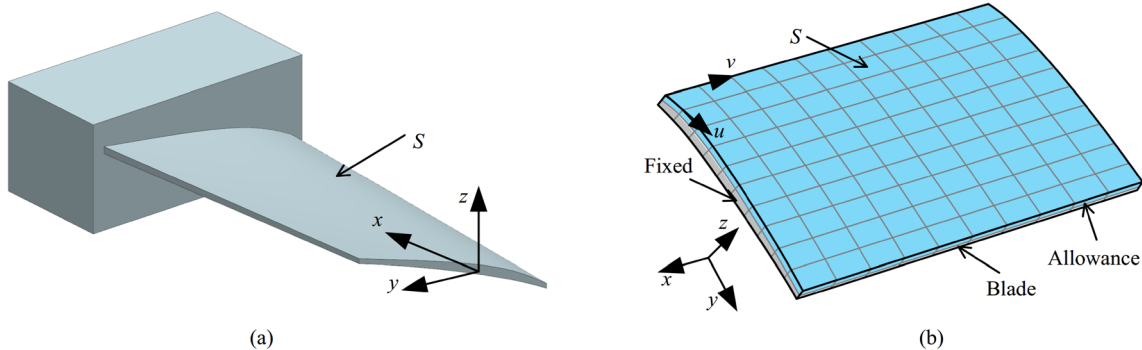


Fig. 3 a The CAD model and b the FE model of the blade

surface, and there is a corresponding relationship between the discrete points $\{P_1, P_2, \dots, P_m\}$ (where m is the total number of the discrete points.) and the nodes $\{N_i, N_j, \dots, N_k\}$. The related deformations are calculated by Eq. (1) or Eq. (5). It should be noticed that the deformation of the discrete point should be caused by the force acting on the same point, and the deformation process is expressed as:

$$K^G \begin{bmatrix} \delta_1 \\ \vdots \\ \delta_i \\ \vdots \\ \delta_n \end{bmatrix} = \begin{bmatrix} 0 \\ \vdots \\ F_i \\ \vdots \\ 0 \end{bmatrix}, \tag{7}$$

where δ_i is the deformation of the discrete point P_i located on the workpiece surface with the node number i under the unit force F_i (see Fig. 4).

Gathering the deformation calculation of all discrete points $S_P = \{P_1, P_2, \dots, P_m\}$ in one matrix, the following expression is obtained.

$$K^G(\delta(P_1), \delta(P_2), \dots, \delta(P_m)) = (F(P_1), F(P_2), \dots, F(P_m)), \tag{8}$$

where $\delta(P_m)$ represents the displacement of all nodes of the workpiece under the force $F(P_m)$. Equation (8) is expanded as follows:

$$K^G \begin{bmatrix} \delta_{11} & \delta_{12} & \dots & \delta_{1m} \\ \vdots & \vdots & \ddots & \vdots \\ \delta_{i1} & \delta_{i2} & \dots & \delta_{im} \\ \vdots & \vdots & \ddots & \vdots \\ \delta_{j1} & \delta_{j2} & \dots & \delta_{jm} \\ \vdots & \vdots & \ddots & \vdots \\ \delta_{k1} & \delta_{k2} & \dots & \delta_{km} \\ \vdots & \vdots & \ddots & \vdots \\ \delta_{n1} & \delta_{n2} & \dots & \delta_{nm} \end{bmatrix} = \begin{bmatrix} 0 & 0 & \dots & 0 \\ \vdots & \vdots & \ddots & \vdots \\ F_{i1} & 0 & \dots & 0 \\ \vdots & \vdots & \ddots & \vdots \\ 0 & F_{j2} & \dots & 0 \\ \vdots & \vdots & \ddots & \vdots \\ 0 & 0 & \dots & F_{km} \\ \vdots & \vdots & \ddots & \vdots \\ 0 & 0 & \dots & 0 \end{bmatrix}, \tag{9}$$

where $\{\delta_{i1}, \delta_{j2}, \dots, \delta_{km}\}$ are the deformations of the nodes $\{N_i, N_j, \dots, N_k\}$ under the forces $\{F_{i1}, F_{j2}, \dots, F_{km}\}$, respectively, which also are the deformations $\{\delta_1, \delta_2, \dots, \delta_m\}$ of the discrete points $\{P_1, P_2, \dots, P_m\}$ of the workpiece surface.

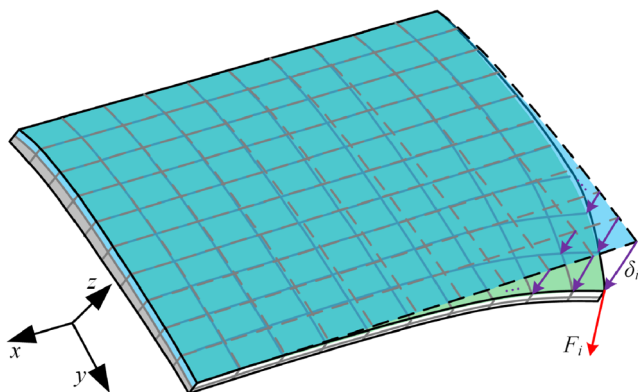


Fig. 4 The deformation of the blade under the force

Through the above definition and calculation, the deformations of the discrete points on the workpiece surface are obtained, and then the deformation of any coordinate located on the workpiece surface is interpolated to establish the deformation field of the whole surface under the unit force. In the meantime, considering that the deformation field is established to describe the deflection trend of the machining surface and the 2-dimensional parameters (u, v) related to the arc length are generally proposed to describe the spatial position of each point on the surface, the coordinates of the points are expressed as $P(u, v) = P(x, y, z)$ (see Fig. 3b), where $(u, v) \in [0, 1]$. Therefore, applying the relationship between the node number and its spatial coordinate, and associating the node deformation and the surface parameters, $\{\delta_1, \delta_2, \dots, \delta_m\}$ can be mapped to $\delta(u, v)$, and the node numbers are ignored.

The specific interpolation methods can be applied to calculate the deformation field such as Lagrange interpolation, Newton interpolation and spline interpolation, and even the surface fitting method for point cloud is considered utilizing the parameters (u, v) and the deformation δ as variables. In particular, the multivariable interpolation should be considered for the 2-dimensional parameter field of in $\delta(u, v)$. Therefore, the bilinear interpolation method is presented as an instance to explain how to interpolate the variables in two directions. Also, the bilinear interpolation method requires discrete points to be distributed in a grid in the parameter domain. Since the FE nodes are presented as the discrete points, the distribution of the discrete points satisfies the requirement of the interpolation method. Therefore, the interpolation formula is expressed as:

$$G(u, v) = \frac{1}{(u_j - u_i)(v_j - v_i)} [u_j - u \quad u - u_i] \begin{bmatrix} \delta(u_i, v_i) & \delta(u_i, v_j) \\ \delta(u_j, v_i) & \delta(u_j, v_j) \end{bmatrix} \begin{bmatrix} v_j - v \\ v - v_i \end{bmatrix}, \tag{10}$$

where $G(u, v)$ is the interpolated deformation field and $\{u_i, u_j, v_i, v_j\}$ is the parameters around the deformation point. It should be noted that the corresponding deformation field $G(u, v)$ is the vector field due to the 3-dimension environment.

In order to analyse the workpiece deformation under the arbitrary cutting force, it is necessary to establish the deformation field of the workpiece surface under the unit force in the x, y, z directions in the workpiece coordinate system. The F_i in Eq. (7) should be replaced as the x, y, z forces, respectively, as shown in the following equations:

$$F_i = \begin{cases} F_x = (1, 0, 0)^T \\ F_y = (0, 1, 0)^T \\ F_z = (0, 0, 1)^T \end{cases}, \tag{11}$$

where F_x, F_y, F_z are the unit forces in x, y, z directions, respectively. The deformation fields $G_x(u, v), G_y(u, v), G_z(u, v)$, also known as the components of the tensor field, are calculated

under the F_x, F_y, F_z force, respectively. The included components in these deformation fields are expressed as:

$$G_i(u, v) = [G_{i,j}(u, v)], \tag{12}$$

where $i, j \in \{x, y, z\}$ and $G_{i,j}$ means the deformation field in direction j under the force in direction i . With these processes, the deformation field of the overall workpiece surface is established.

3.2 The deflection error model of the thin-walled part milling process

To describe the machining error of the workpiece, the measurement data and the design model are select to compare the deviation which is known as the machining error, and the orientation of the deviation calculation is regarded as the normal direction of the corresponding point in the design model. It can be concluded that only the displacement in the normal direction of the geometric model is recognized as the elastic deformation

error. The deformation field G_i from Eq. (12) has been defined as the deflection under the unit force from Eq. (11). Therefore, combined with the distribution of the workpiece deformation field and the cutting force acting on the workpiece, the machining deformation error D is calculated by:

$$D = G_n^T F = G_{x,n} F_x + G_{y,n} F_y + G_{z,n} F_z, \tag{13}$$

where $G_n = [G_{x,n}, G_{y,n}, G_{z,n}]^T$ and $G_{x,n}, G_{y,n}$ and $G_{z,n}$ are the deformation fields (see Fig. 5a, b, c) in the normal direction caused by the unit force in the x, y and z directions, respectively, which are calculated by:

$$G_{m,n} = N^T G_m = n_x G_{m,x} + n_y G_{m,y} + n_z G_{m,z}, \tag{14}$$

where $m \in \{x, y, z\}$, $N = [n_x, n_y, n_z]^T$ is the normal direction of the workpiece.

Similarly, the deformation field (see Fig. 5d) in the normal direction of the workpiece caused by the unit force of the normal direction is calculated by:

$$G_{n,n} = N^T G_n. \tag{15}$$

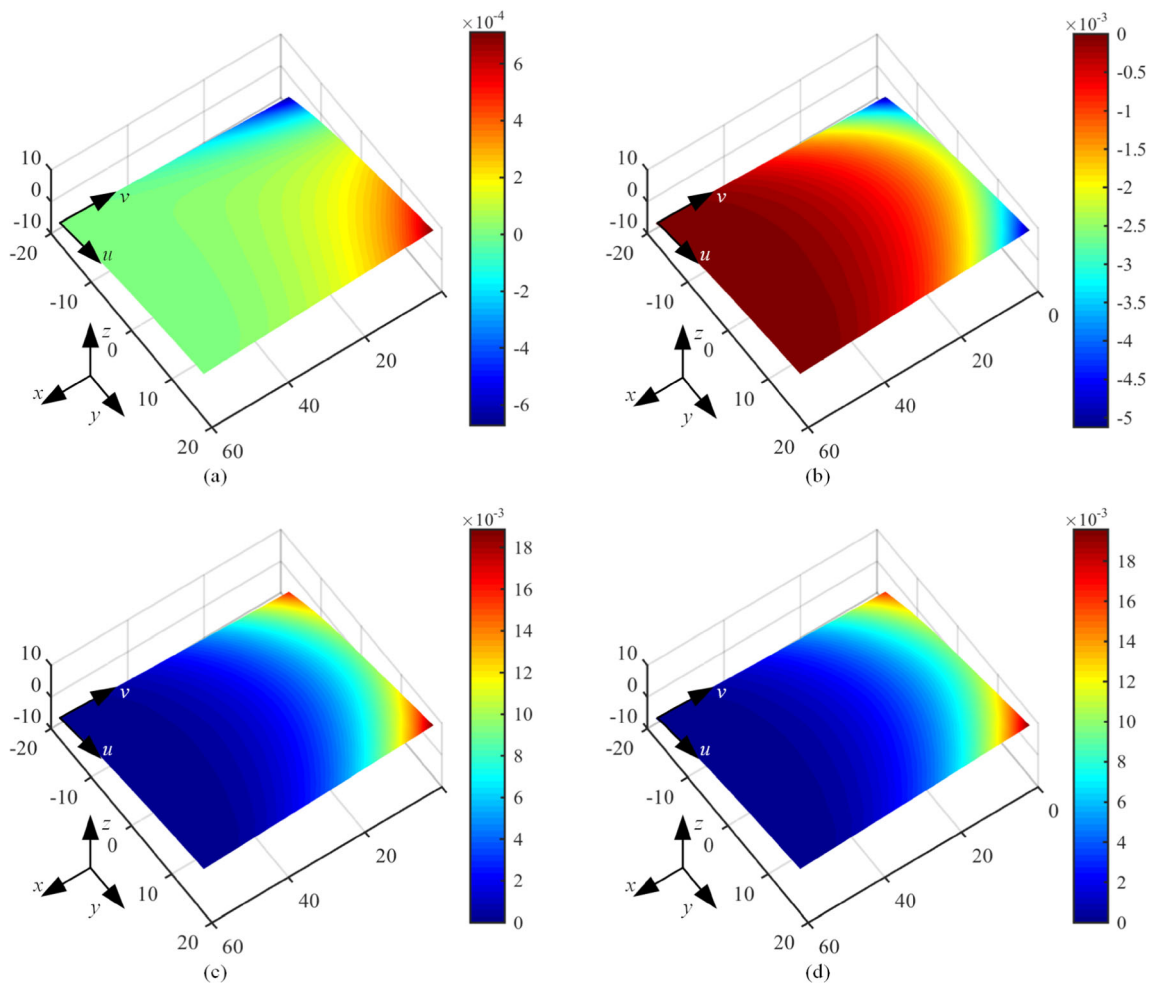


Fig. 5 The deformation fields in normal direction caused by the unit forces of a direction x , b direction y , c direction z and d normal direction (unit: mm)

3.3 The cutting path planning method based on the stable-state deformation field

Combined with the deformation error model of the thin-walled milling process, the cutting path with less deformation error will be planned in this section.

To describe the variation trend of the workpiece deformation field caused by different material removal sequences, the deformation of each point in the surface should be determined with respect to the specific cutting sequence during the milling process. And the deformation of the overall machining process in every moment should be added together to evaluate the final machining error. Therefore, the concepts of the trend of the point deformation and the total deformation of the target surface of the workpiece are introduced to achieve the above calculation.

First, the cutting sequence is expressed with a defined order of all the CC points. The CC points from the discrete point set $\{P_1, P_2, \dots, P_m\}$ in Eq. (6) are sorted by the corresponding order based on the specific cutting path planning strategy. The sequence vector CP of the cutting path is defined as:

$$CP = [P_i, P_j, \dots, P_k], \tag{16}$$

where P_i, P_j and P_k represent the coordinate of the CC points in the sorted order. Therefore, the CC points in the moment s ($s = 0, 1, \dots, m$) of the cutting sequence are expressed as $CP(s) = P_i$. The cutting is not performed when $s = 0$. It should be noticed that CP is one of the cutting paths from the functional space $F[CP]$.

With these definitions, the deformation of the point during the milling process is expressed as $D(CP, CP(s_c), s)$ that means the deformation error from Eq. (13) in the moment s of the cutting sequence CP , and s_c is the specific moment of the cutting sequence to confirm the cutting position. When $s = 0$, $D(CP, CP(s_c), 0)$ will be zero. Furthermore, if $CP(s_c)$ is cut (also means $s > s_c$), the corresponding deformation $D(CP, CP(s_c), s)$ will be zero in the rest milling process. The deformations of different CC points during the milling process are demonstrated in Fig. 6. The blue and green lines show the deformation trends of $CP_1(s_1)$ and $CP_1(s_2)$ with respect to CP_1 and s . Furthermore, the deformations of these points remain constant until the points are cut. It could be confirmed that the milling process for $CP_1(s_1)$ and $CP_1(s_2)$ is stable before s_1 and s_2 . The purple line shows the deformation trend of $CP_2(s_3)$ with respect to CP_2 and s . The deformation is increased for the unstable milling process of CP_2 .

Then, the total deformation of the workpiece surface is introduced to represent the summation of the deformations of all sampled CC points on the workpiece, which is expressed as:

$$q = \sum_{s=0}^m D(CP, CP(s), s), \tag{17}$$

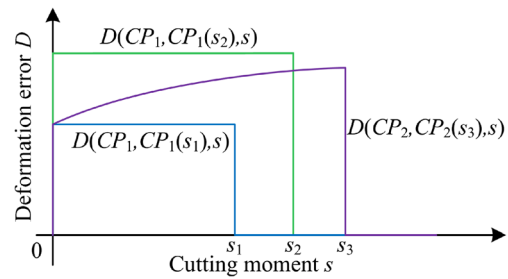


Fig. 6 Deformation errors of the points

where q is the total deformation amount of the workpiece surface. To achieve the minimum deformation error of the milling process, the cutting sequences from $F[CP]$ are implemented. The minimization problem is set as:

$$\min q = \sum_{s=0}^m D(F[CP], F[CP(s)], s). \tag{18}$$

Considering that the corresponding cutting parameters are not proposed currently, the cutting force conditions of each CC point cannot be accurately determined. Therefore, the normal deformation field $G_{n,n}$ (see Fig. 5d) under the normal unit force is applied as the reference deformation field G for the deformation calculation. It should be noticed that $G_{n,n}$ varies during the milling process. The new deformation field of the workpiece should be updated with respect to the moment of the cutting sequence for a more accuracy calculation process. However, the varied deformation field could be replaced by the initial $G_{n,n}$ to simplify the calculation process due to the time-consuming reason. Hence, the minimization problem of q is not suitable for the minimum deformation error of the milling process, and the trend of the local deformation $q(s)$ is developed. As the material is removed, the deformation of the remaining workpiece is changed. Combined with the definition of the deformation of the point during the milling process, the material that has been cut will be ignored when calculating $q(s)$, and Eq. (17) is updated as follows:

$$q(s) = \sum_{i=s}^m G(CP, CP(i)). \tag{19}$$

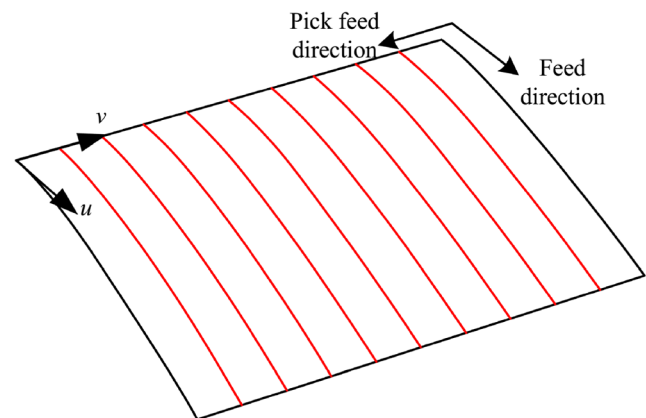


Fig. 7 Cutting path of $Path_1$

Combining the trend function of the local deformation with respect to the moment of the cutting sequence and the feature that the high stiffness region can improve the cutting performance by supporting the cutting process of the low stiffness region based on the stiffness matrix, the deformation amount of the uncut region is added to calculate the integrated cutting process deformation Q which is expressed as:

$$Q = \sum_{s=0}^{n_s} q(s). \tag{20}$$

Taking the blade model shown in Fig. 3 as an instance, since different cutting paths lead to different Q , the detailed cutting paths are introduced. Considering the continuity of the cutting path, two common cutting paths which are parallel inward path $Path_1$ (feed in direction u and pick feed in direction v) and vertical inward path $Path_2$ (feed in direction v and pick feed in direction u) with similar cutting parameters (such as axial depth of cut, radial depth of cut and orientation of tool axis.) [26] are introduced. The cutting lines of both tool paths are shown in Figs. 7 and 8, respectively. The local deformation $q(s)$ and the integrated cutting process deformation Q are calculated according to Eqs. (19) and (20), resulting in Fig. 9. From this figure, when the larger deflection area is cut primarily, the subsequent total deformation amount will decrease sharply, which leads to a relatively small Q . On the other hand, if the larger deflection area is not preferentially removed, the subsequent total deformation amount will gradually decrease, resulting in a relatively large Q .

Therefore, $Path_1$ is verified theoretically as a better material removal sequence based on the stable-state deformation field.

4 The prediction of the cutting force corresponding to radial depth of cut

4.1 The cutting force model for ball-end milling

During the milling process, the cutting force plays a significant role affecting the machining deformation, vibration,

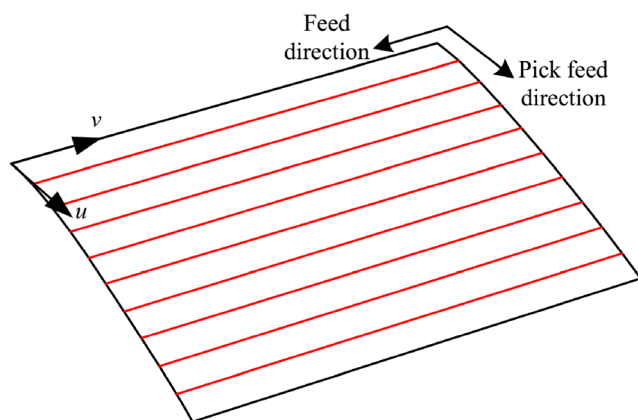


Fig. 8 Cutting path of $Path_2$

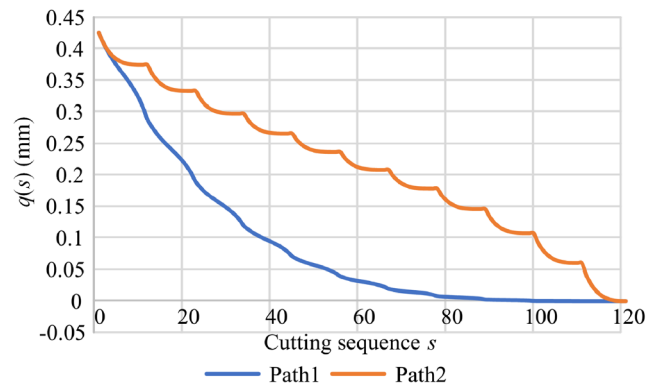


Fig. 9 The local deformation amount and its trend

cutting heat, tool life and cutting condition monitoring. Especially in the thin-walled part milling process studied in this paper, the cutting force is the main factor causing the workpiece deformation. At present, the research on cutting force modelling is relatively mature. The mechanistic cutting force model in ball-end milling is applied in this paper as follows.

Firstly, the geometric model of the ball-end cutter is established as shown in Fig. 10. The axis tz is set along the direction of the tool axis, and the tx and ty axes are settled in the boundary plane between the ball part and the cylindrical part of the ball-end cutter. Furthermore, the tool coordinate system $txyz$ is resulted. In this coordinate system, the cutting edge is expressed as the green curve, and the rotation angle φ and the immersion angle κ are introduced to describe the position of the point in the cutting edge. Applying the cutting force model, the differential tangent dF_t , radial dF_r and axial dF_a cutting forces acting on an infinitesimal cutting edge segment can be calculated as follows:

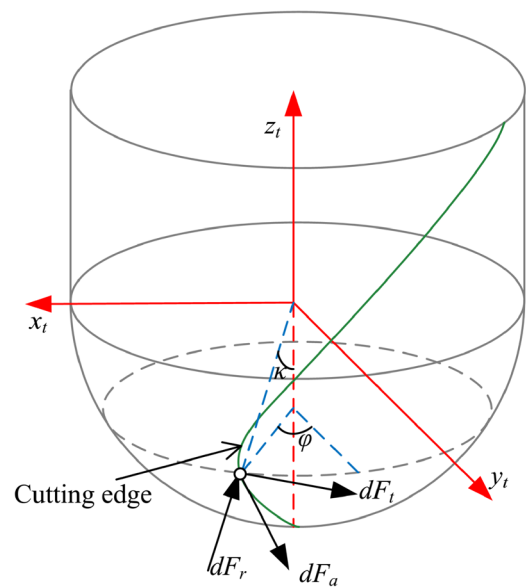


Fig. 10 Geometric model of the ball-end mill cutter and the cutting force components

$$dF_i(\varphi, z) = K_{ic}H(\varphi, \kappa)db(z) + K_{ie}ds(z), \tag{21}$$

where $i \in \{t, r, a\}$, K_{ic} and K_{ie} are the shear force coefficients and the edge cutting coefficients, respectively, $H(\varphi, \kappa)$ is the chip thickness and db and ds are the chip width and cutting edge length, respectively.

Decomposing the above cutting force into the x_t , y_t and z_t directions, the cutting forces in the tool coordinate system TCS are evaluated by applying the transformation matrix, as in the following equation:

$$\begin{bmatrix} dF_{xt} \\ dF_{yt} \\ dF_{zt} \end{bmatrix} = \begin{bmatrix} -\cos \varphi & -\sin \kappa \sin \varphi & -\cos \kappa \sin \varphi \\ \sin \varphi & -\sin \kappa \cos \varphi & -\cos \kappa \cos \varphi \\ 0 & \cos \kappa & -\sin \kappa \end{bmatrix} \begin{bmatrix} dF_t \\ dF_r \\ dF_a \end{bmatrix}. \tag{22}$$

Then, the total cutting forces acting on the cutting tool are evaluated by integrating the cutting force in the entire cutting edge and adding the cutting force at the corresponding position in each cutting edge, as in the following equation:

$$F_t = \sum_{j=1}^{n_t} \int_{z_1}^{z_2} dF_{t,j} dz, \tag{23}$$

where $F_t = [F_{xt}, F_{yt}, F_{zt}]^T$, j is the cutting edge number, n_t is the total number of the cutting edges and z_1 and z_2 are the upper and lower bounds of the cutting area in the tool axis direction in the milling process.

The average cutting force is used to identify the cutting force coefficients of TC4 cutting process, and a 4-tooth ball-end cutter with 12-mm diameters is afforded. Since the diameter of ball-end cutter changes in the direction of tool axis, the corresponding cutting edge is in different shapes, which will affect the cutting force coefficients of each layer [27]. Therefore, the difference of cutting forces in axis height is needed to determine the cutting coefficients function of axial height. In order to simplify the calculation, the slot milling is adopted. The spindle speed is 1061 rev/min, and the feed per tooth is 0.02, 0.04 and 0.06 mm/tooth. The differences of the

Table 1 The difference of average cutting force in axis height

Axis height (mm)	F_x (N)	F_y (N)	F_z (N)
0.25	-9.303	42.919	37.734
0.50	-12.341	36.292	27.944
0.75	-22.641	39.920	48.778
1.00	-13.927	33.211	14.203
1.25	-12.624	34.205	14.891
1.50	-18.625	32.851	6.408
1.75	-11.059	31.405	17.721
2.00	-18.077	29.305	6.269
2.25	-9.766	30.641	2.000
2.50	-21.607	31.998	1.175

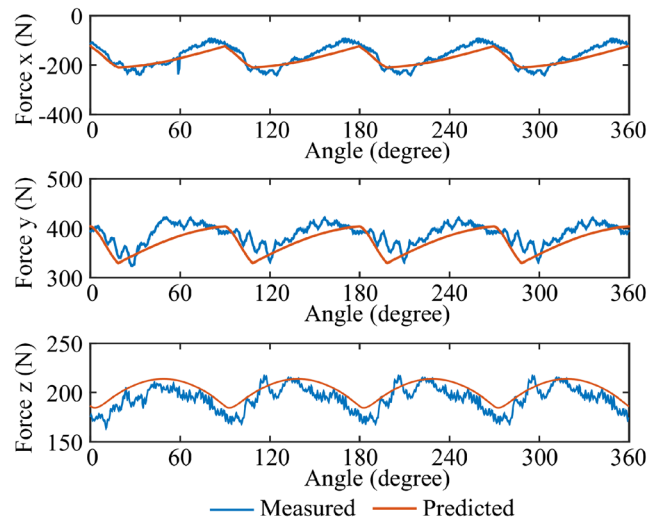


Fig. 11 The measured and predicted cutting forces

average cutting forces relating to the axial depth of cut are shown in Table 1 when the feed per tooth is 0.06 mm/tooth.

The cutting coefficients function of axial height a_p are shown in the following:

$$\begin{cases} K_{tc} = -167.21a_p^2 - 695.10a_p + 2428.48 \\ K_{rc} = -2.98a_p^3 + 553.30a_p^2 - 2018.64a_p + 2263.04 \\ K_{ac} = -203.18a_p^3 + 923.66a_p^2 - 1189.81a_p + 740.01 \\ K_{te} = -0.06a_p^3 - 3.42a_p^2 + 11.60a_p + 2.48 \\ K_{re} = -0.13a_p^3 - 4.44a_p^2 + 15.03a_p + 4.76 \\ K_{ae} = 0.10a_p^3 - 0.13a_p^2 + 1.81a_p - 0.17 \end{cases} \tag{24}$$

The measured average cutting forces in x , y and z axes are -163.88, 385.71 and 188.02 N, respectively, when the axis depth of cut is 2.75 mm and the feed rate per tooth is 0.06 mm/

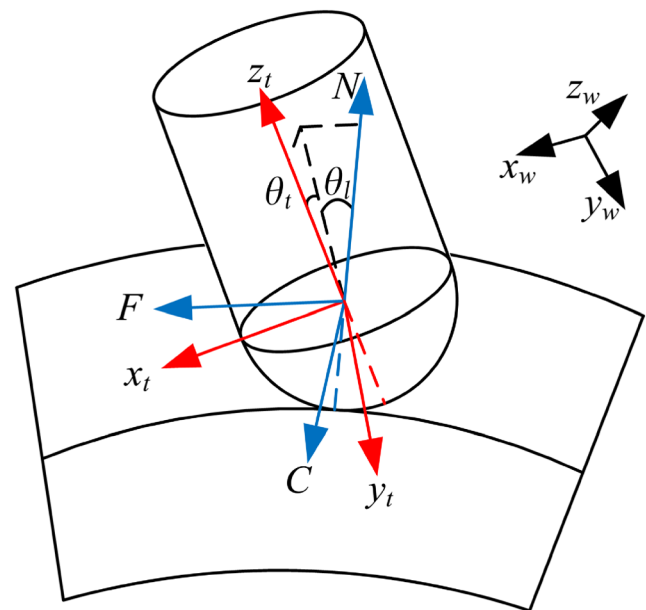
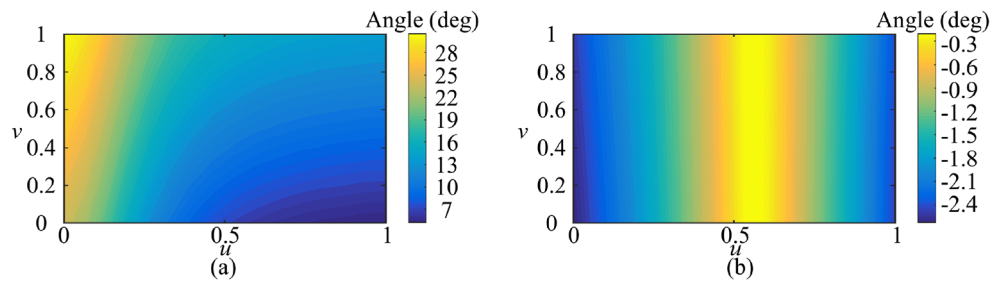


Fig. 12 The state of the ball-end tool and workpiece milling process

Fig. 13 The distribution of **a** lead and **b** tilt angle



tooth. Applying the proposed cutting force model, the predicted average cutting forces in x , y and z axes are -174.43 , 371.51 and 201.10 N, respectively. The dynamic cutting forces in a rotation period are shown in Fig. 11. The corresponding errors are 6.44 , -3.68 and 6.95% which demonstrate the effectiveness and precision of the proposed ball-end cutting force model.

4.2 The relationship between the cutting force and radial depth of cut

When machining the free-form surface with ball-end mill, the local coordinate system is introduced in the CC points to describe the orientation of the cutter, consisting of feed (F), cross-feed (C) and surface normal (N) axes. The lead angle θ_l is the rotation of the tool axis about the cross-feed axis (C) and the tilt angle θ_t is the rotation about the feed axis (F). TCS is the tool coordinate system which is the rotated form of the FCN. The cutting force from Eq. (23) is in TCS. And a fixed coordinate system, WCS, is the workpiece coordinate system which is built to describe the CC points in the workpiece. These coordinate systems and their relations are shown in Fig. 12.

Based on the classical cutting force model, the variation of the cutting force acting on the cutting tool with the spindle rotation in the tool coordinate system TCS is analyzed. Considering that the milling process is cyclically variable and the spindle speed is particularly fast compared to the feed rate, the average force over the period can be utilized to indicate the equivalent force causing the elastic deformation of the workpiece during this period [21]. In addition, the coordinate transformation is necessary to calculate the cutting force acting on the workpiece in WCS by analysing the difference

between the tool and workpiece coordinate systems shown in Fig. 12. Comprehensively, the equivalent cutting force acting on the workpiece is expressed as:

$$F_w = \frac{1}{2c\pi} \int_0^{2c\pi} T F_t d\varphi, \tag{25}$$

where c is the period amount which is confirmed by the range of integration, F_t is the cutting force and T is the transformation matrix which is determined by the relation between the TCS and WCS.

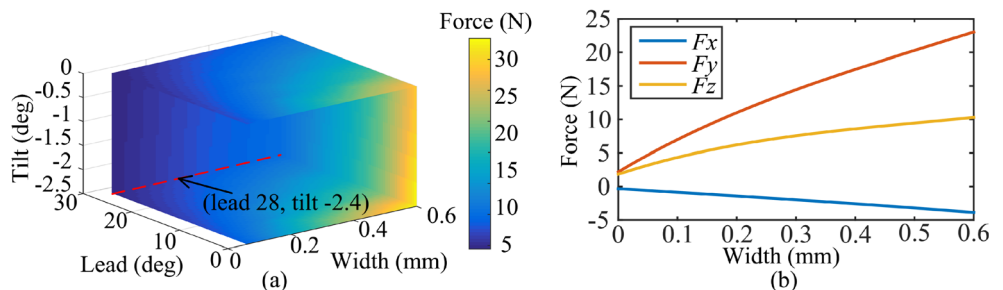
However, the tool axis is different from the surface normal when milling the blade presented in Fig. 3 in z axis. The influence of the lead and tilt angles should be considered. Figure 13 shows the distributions of the lead and tilt angles of the proposed blade.

Since the tool axis is changed, the CC area in FCN and TCS can be transformed using the following equation.

$$TCS = \begin{bmatrix} \cos \theta_l & 0 & \sin \theta_l \\ \sin \theta_l \sin \theta_t & \cos \theta_t & -\sin \theta_t \cos \theta_l \\ -\cos \theta_l \sin \theta_t & \sin \theta_t & \cos \theta_t \cos \theta_l \end{bmatrix} FCN. \tag{26}$$

Based on the above preparation, the new CC area in TCS and the changed feed vector are afforded to the cutting force model. The axis depth of cut is 1 mm and the feed per tooth is 0.06 mm/tooth. The average cutting force function of radial depth of cut (width), lead and tilt angle in WCS is constructed as $F_w = f(a_e, \theta_l, \theta_t)$ and the z force function is shown in Fig. 14a. The red dotted line in this figure shows the relationship between z force and the radial depth of cut when $\theta_l = 28^\circ$ and $\theta_t = -2.4^\circ$. In this condition, the cutting force function $F_w = f(a_e)$ of width a_e in different axes is shown in Fig. 14b.

Fig. 14 **a** The cutting force function in z axis corresponding to parameters and **b** the relationship between cutting forces and radial depth of cut



5 The radial depth of cut optimization of the tool path

Based on the analysis and calculation of the stable-state deformation field, the material removal sequence with less deformation, known as the parallel inward path $Path_1$, is chosen, which removes the low stiffness area preferentially. However, even with this cutting path, the deformation of the low stiffness region is still out of range since the same cutting parameters are performed around the whole surface. Therefore, it is necessary to optimize the cutting parameters of the local area to ensure that the deformation of each point on the workpiece is as small as possible.

Although the cutting force is calculated by a combination of the cutting force coefficients, the chip width and the edge length in the cutting force model, only the axial depth of cut, the radial depth of cut, the tool axis orientation, the spindle speed and the feed rate are concerned to determine the cutting force in tool path planning process. This section mainly considers how the radial depth of cut influences the cutting force while keeping the axial depth of cut, the spindle speed and the feed rate constant. And the tool axis is varying when machining the free-form surface with 3-axis machine tool. Therefore, the equivalent cutting force in Eq. (25) is expressed as $F_w(a_e)$ where θ_p, θ_t are specific for each CC point according to Fig. 13 and Fig. 14. Considering the deformation calculation from Eq. (13) and the research of the material removal sequence in the former section, the deformation of each point on the workpiece could be reduced when the cutting force decreases with the stable-state material removal sequence. However, it is impossible to blindly reduce the cutting parameters and decrease the machining efficiency. In addition, considering the disadvantages of excessive cutting force, such as tool life, tool deformation, stability of the machine tool and the cutting process, excessive cutting parameters are not recommended. Especially in the free-form surface milling process with ball-end cutter, the maximum cutting width of each CC point, also known as the maximum radial depth of cut $a_{e, max}$, should be

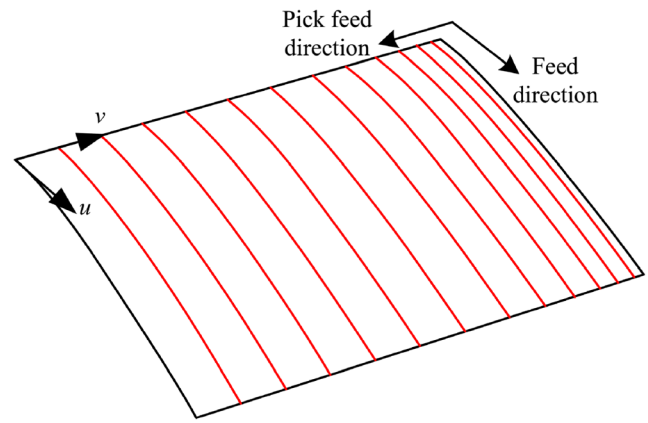


Fig. 16 Cutting path of $Path_3$

chosen carefully to ensure that the scallop height after cutting is within the threshold. Generally, the cutting force calculated with the maximum radial depth of cut can stay in the range of the maximum cutting force. To be on the safe side, the proper parameters should be determined when planning the original cutting path before the optimization.

Combining the above analysis and the deformation error of the workpiece from Eq. (13), the optimization method for the radial depth of cut of the cutting path is expressed as:

$$d_{max} = D(u, v) = \mathbf{G}_n^T(u, v) \mathbf{F}_w(a_e), \tag{27}$$

$$a_{e, real} = \min\{a_{e, max}, a_{e, cal}\}, \tag{28}$$

where d_{max} is the maximum deformation of the workpiece, $a_{e, real}$ is the optimized radial depth of cut and $a_{e, cal}$ is the radial depth of cut that satisfies the deformation error model and also is the solution of a_e in Eq. (27). The specific calculation process refers to the solution of nonlinear equation.

5.1 The optimization of the parallel inward path

For the parallel inward path $Path_1$, only the distance of the adjacent cutting lines is calculated when optimizing

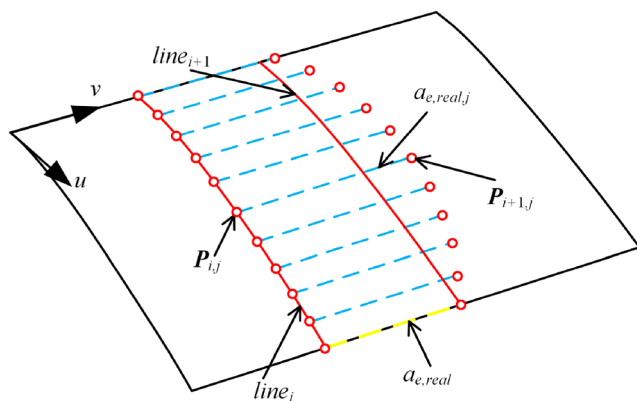


Fig. 15 The general optimization method for parallel inward path

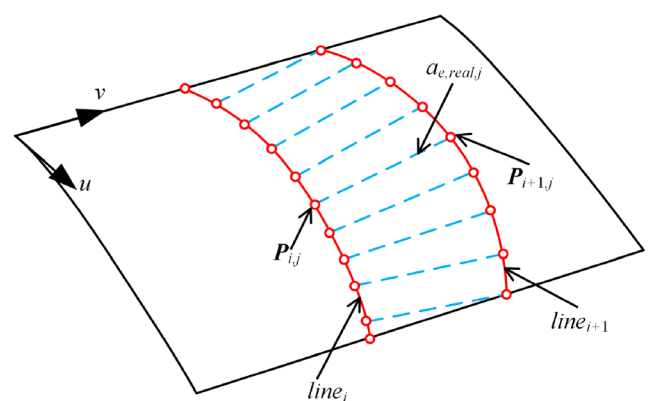


Fig. 17 The general case of the single-point optimization algorithm

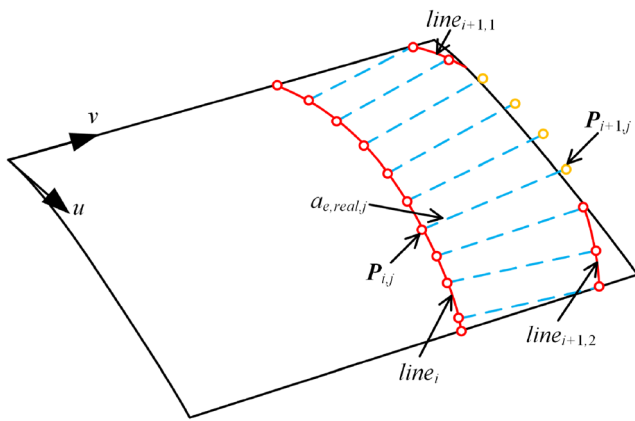


Fig. 18 The degenerate case of the single-point optimization algorithm

the radial depth of cut to ensure the cutting path is fed in the direction of parameter u . The following algorithm is developed as shown in Fig. 15. Firstly, the discrete points $P_{i,j}$ (i is the cutting line number, and j is the CC point number) are sampled from the current cutting line $line_i$. Then, the radial depths of cut $a_{e,real,j}$ and the corresponding CC point $P_{i+1,j}$ under the conditions from the Eqs. (27) and (28) are calculated. Finally, the minimum value of these radial depths of cut is the optimized radial depth of cut of the adjacent cutting line $line_{i+1}$ by $a_{e,real} = \min(a_{e,real,j})$. Applying the algorithm to the target surface, the optimized parallel inward cutting path $Path_3$ is obtained (see Fig. 16).

5.2 The single-point optimization algorithm

In the above algorithm of optimizing $Path_1$, the minimum value of the optimized radial depths of cut of all CC points is regarded as the optimal radial depth of cut to ensure that the cutting path is still parallel and inward after optimizing. In other words, the independent feature of each point is ignored when the width of each

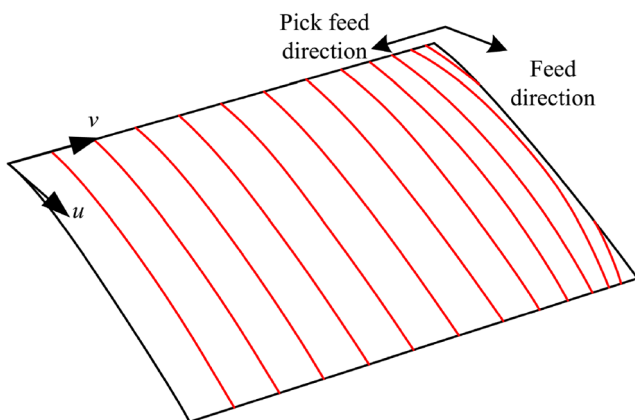


Fig. 19 Cutting path of $Path_4$

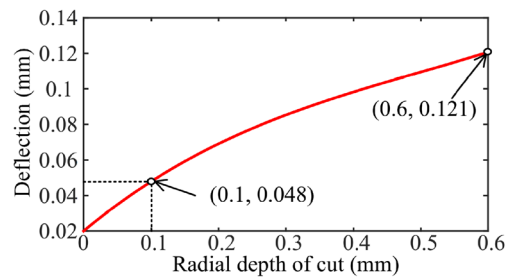


Fig. 20 The relationship between springback and the radial depth of cut

CC points is reduced to the width of the lowest stiffness point in the current cutting line. Therefore, each CC point can be optimized if ignoring the parallel constraint of cutting path.

In order to maintain a better material removal sequence in the cutting process, the low stiffness region should be removed first. According to the generation method of material removal sequence (see Ref. [21, 25]), the largest stiffness region, also is the fixed end, is regarded as the initial value to plan the allowance distribution order of the remaining workpiece, and the reverse order of the allowance distribution is the cutting sequence in the machining process. Therefore, the relevant algorithm is designed as follows (see Fig. 17). Firstly, the discrete points $P_{i,j}$ are sampled from the current cutting line $line_i$. Then, the radial depths of cut $a_{e,real,j}$ and the corresponding CC point $P_{i+1,j}$ under the conditions from the Eqs. (27) and (28) are calculated, and these CC points $P_{i+1,j}$ are fitted to construct the adjacent cutting line $line_{i+1}$. However, the degenerate case occurs when the planned tool path is close to the edge of the low stiffness region. As a result, the optimized CC points are out of the surface range of the workpiece (see the yellow points in Fig. 18). In this situation, the overstep points will be removed from the optimized CC points set. The rest CC points constitute their cutting lines in the corresponding position, which are the $line_{i+1,1}$ and $line_{i+1,2}$ in Fig. 18.

It should be noted that the cutting path formed by the calculated CC points with the optimized radial depth of cut may not be smooth. The application of the curve fitting method is needed to relocate the CC point. As a result, the requirement of the deformation error control and the smoothness of the cutting path are satisfied. The

Table 2 The relevant machining data

	$Path_1$	$Path_2$	$Path_3$	$Path_4$
Length of cutting path/mm	3781.92	3781.37	4677.58	3891.63
Number of cutting rows	100	62	124	135
Total time/s	547.102	490.044	677.146	611.121
Average error/mm	0.0438	0.0992	0.0337	0.0323
Maximum error/mm	0.1443	0.5107	0.0898	0.1099

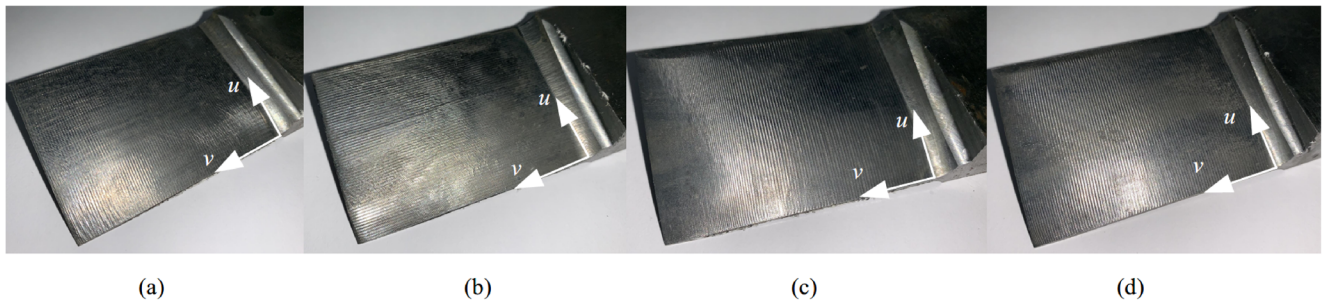


Fig. 21 The blades after machining with **a** $Path_1$, **b** $Path_2$, **c** $Path_3$ and **d** $Path_4$

final tool path applying the single-point optimization algorithm is shown in Fig. 19.

6 Experiments and verification

6.1 The preparations of the machining process

To verify the material removal sequence and the cutting path optimization method based on the stable-state deformation field

proposed in this paper, the thin-walled blades machining experiments are designed. The dimensions of the blade are about $60 \times 40 \times 1$ mm shown in Fig. 3a. Four cutting paths proposed in this paper are applied to the blade machining experiments.

The experiments are prepared as follows: a ball-end cutter with diameter 12 mm is applied in the machine tool YHVT850 to cut the TC4 workpiece. The cutting parameters are set as the following: spindle speed is 3000 rpm, feed rate is 700 mm/min, workpiece allowance is 1 mm, maximum cutting width is 0.6 mm and

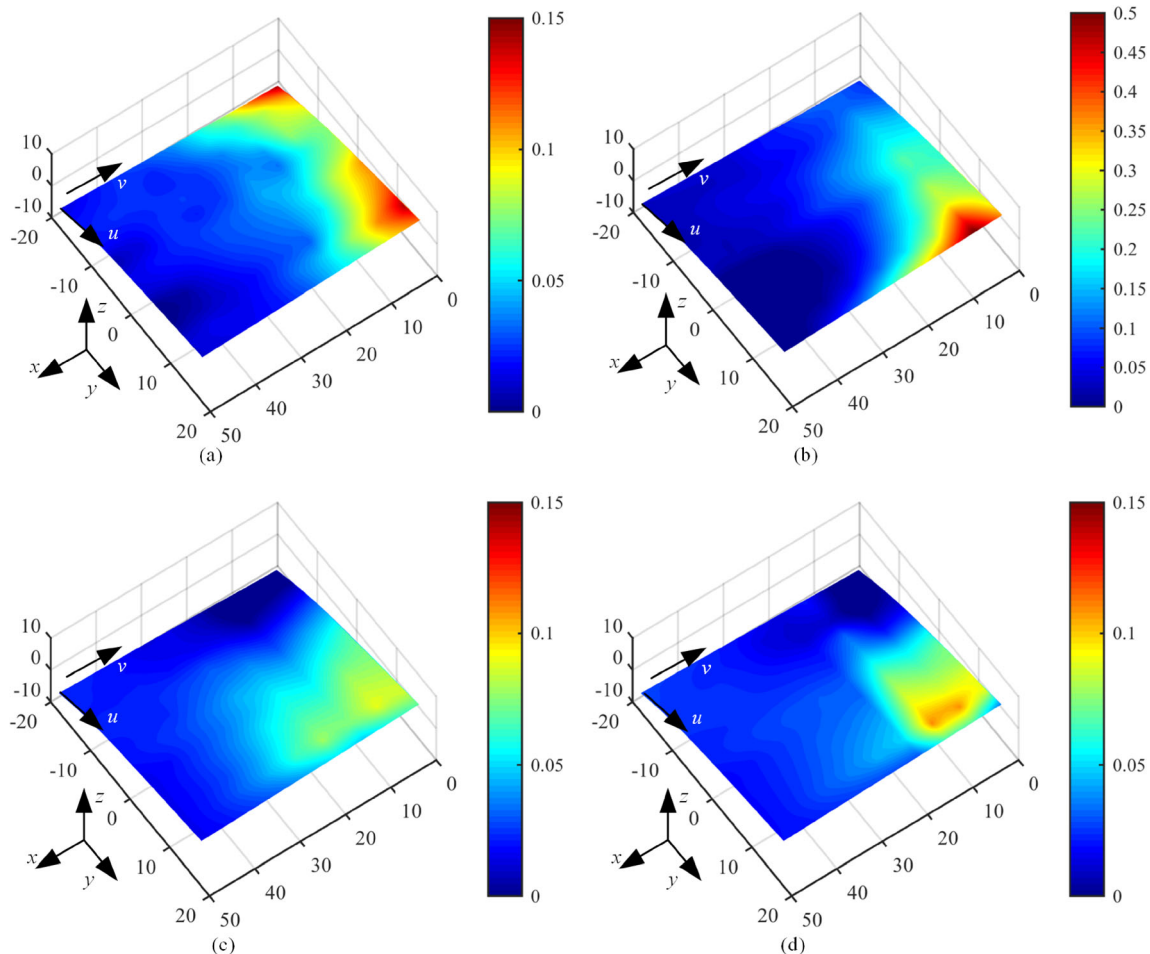


Fig. 22 The cloud figures of machining error (mm) distribution of **a** $Path_1$, **b** $Path_2$, **c** $Path_3$ and **d** $Path_4$

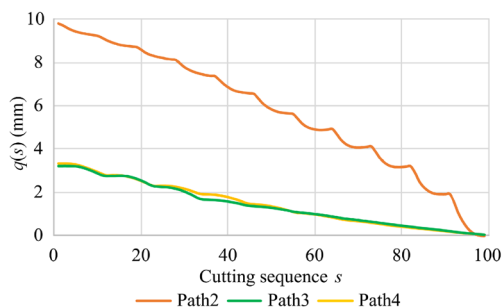


Fig. 23 The local deformation amounts of Path₂, Path₃ and Path₄

tool axis is in direction z . Four cutting paths are shown in Figs. 7, 8, 16 and 19. The tolerance is 0.05 mm according to the compressor blade machining process.

In order to verify the effectiveness of the proposed algorithms, the conservative machining parameters are selected to avoid the negative factors of the machining process, such as chatter. Also, in order to decrease the influence of the scallop height caused by the ball-end milling, the maximum cutting width 0.6 mm is set when designing the cutting paths, and the scallop height of the entire machining surface is under 0.01 mm.

For Path₃ and Path₄, Section 5 shows how to optimize radial depth of cut of the cutting path. The lowest stiffness region known as the blade tip is taken as an example to calculate the optimized radial depth of cut. The cutting force function of radial depth of cut is generated according to Section 4. Meanwhile, the deflection of the tip region from the deformation field is -0.000308 , -0.002786 and 0.009969 mm/N when the allowance is 1 mm. Applying Eqs. (13) and (27), the relationship between deflection of the blade and radial depth of cut is obtained as shown in Fig. 20. The deformation error is out of tolerance when the radial depth of cut is 0.6 mm which is the maximum radial depth of cut $a_{e, max}$. A new radial depth of cut $a_{e, cal} = 0.109$ mm is the solution of Eq. (27) when $d_{max} = 0.05$ mm. Therefore, $a_{e, real}$ is set as 0.1 mm for convenience and the deflection is 0.048 mm which is lower than the tolerance. For the root region of blade, the deformation field is much smaller, which leads to a larger radial depth of cut, larger than $a_{e, max}$. The $a_{e, real}$ value in these

regions is $a_{e, max}$. Therefore, the range of the optimized radial depth of cut for Path₃ and Path₄ is [0.1,0.6].

6.2 The machining errors of the proposed cutting paths

Before the milling process, the lengths of four cutting paths are calculated as shown in Table 2 before the milling process. It is obvious that the lengths of Path₁ and Path₂ are nearly the same when the same maximum cutting width is set. Since the cutting width is reduced in the low stiffness region and the parallel cutting feature is reserved, the length of Path₃ is the longest and longer than Path₁ by 23.7%. At last, the cutting width of the larger stiffness region is not reduced to the value of the lowest stiffness position of the current cutting line in the cutting path Path₄. Therefore, the final length of the Path₄ is not too long and is only longer than Path₁ by 2.9%.

Afterwards, four different cutting paths are implemented in the workpiece machining process, and the final machining results are shown in Fig. 21, and the total machining time is shown in Table 2. Considering that the non-cutting moves such as the engage and retract movements are significant to connect different cutting lines, therefore, the excessive number of cutting lines which cause frequent engage and retract and even the traversal movements will affect the final machining time. It can be found from Table 2 that the machining time of Path₂ is reduced by 10.4% comparing to Path₁ and the machining times of Path₃ and Path₄ are increased by 23.8 and 11.7%, respectively.

For these machined blades, the dimensions are measured to calculate the machining errors and plot the cloud figures (see in Fig. 22) under clamping condition. After analysing the machining errors (where the average and maximum errors are shown in Table 2) and the distributions, it could be concluded as follows:

- 1) The machining error of Path₂ is largest, the average error is 2.264 times of Path₁, and the maximum error is 3.539 times of Path₁. It could be concluded that removing the

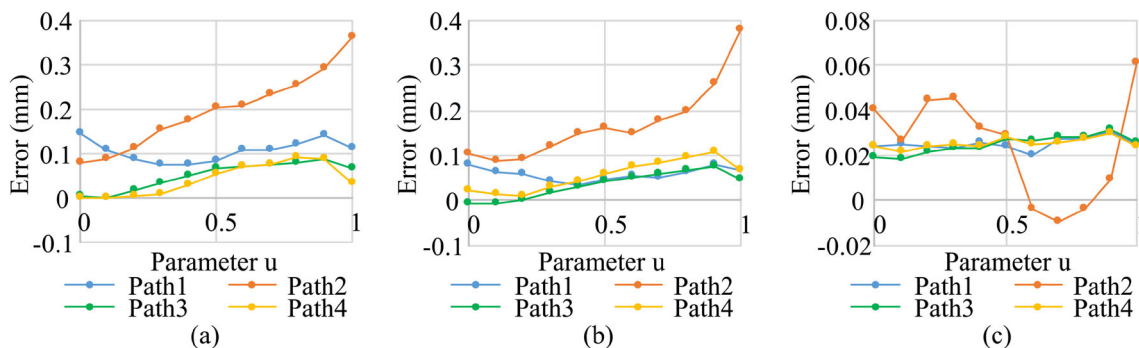


Fig. 24 The machining errors of the sections a $\nu = 0.97$, b $\nu = 0.77$ and c $\nu = 0.37$ applied different cutting paths

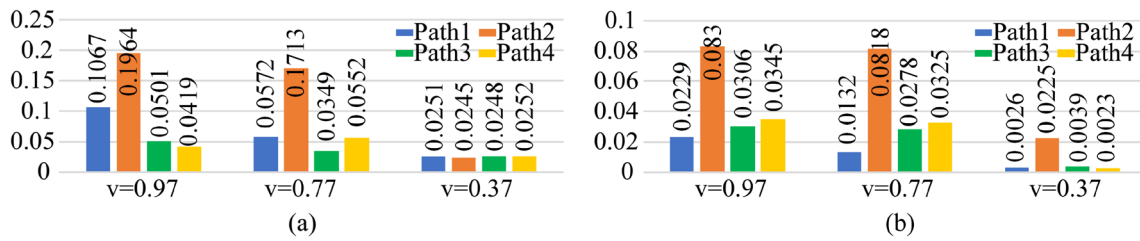


Fig. 25 a The average errors (mm) and b standard deviations (mm) of three sections

low stiffness region preferentially can lead to a smaller machining error.

- 2) Comparing to *Path*₁, the average errors of *Path*₃ and *Path*₄ are reduced by 23.1 and 26.3%, respectively, and the maximum errors are reduced by 37.7 and 23.8%, respectively. It could be concluded that the optimized cutting path can reduce the machining error effectively.

Besides, the local deformation amounts of *Path*₂, *Path*₃ and *Path*₄ are compared in Fig. 23. Due to the severe variation of the deformation field when milling the blade in *Path*₂, the local deformation amount of each cutting moment is larger than that in *Path*₃ and *Path*₄. It demonstrates that the optimized cutting paths, *Path*₃ and *Path*₄, can lead to a smooth decrease of local deformation amount.

However, since the analysis of the error clouds only considers the variation of the overall error while the optimized cutting lines are located in the low stiffness region, it is necessary to compare the machining errors of the optimized regions to demonstrate the effectiveness of the optimization algorithm. Analysing the optimized cutting paths of *Path*₃ and *Path*₄, it could be found that the optimized region locates in $v \in [0.7, 1]$. Therefore, the sections $v = 0.97$ and $v = 0.77$ (also are the sections $x = 2$ and $x = 14$, respectively) are selected to verify the effectiveness of the optimization algorithm, and the section $v = 0.37$, known as the section $x = 38$, in the non-

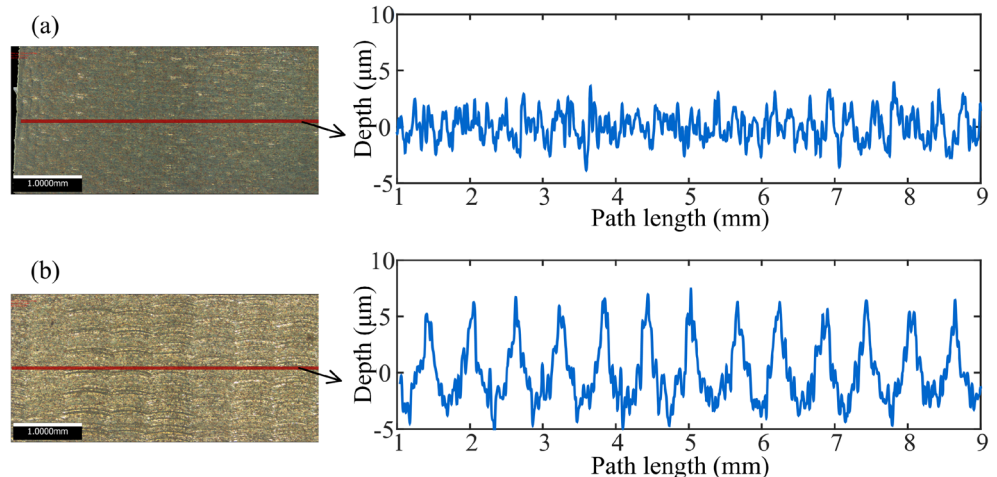
optimized region is proposed as the contrast. The errors of these sections are shown in Fig. 24, and the average errors and the standard deviations are shown in Fig. 25.

In section $v = 0.97$, comparing to *Path*₁, the average errors of *Path*₃ and *Path*₄ are reduced by 53.0 and 60.7%, respectively. In section $v = 0.77$, comparing to *Path*₁, the average errors of *Path*₃ and *Path*₄ are reduced by 39.0 and 3.5%, respectively. In section $v = 0.37$, the average errors of *Path*₃ and *Path*₄ are 98.8 and 100.4% of *Path*₁, respectively. Most regions with excessive errors are corrected by applying *Path*₃ and *Path*₄, which results in larger standard deviations. These data demonstrate that the optimization algorithm of the radial depth of cut can reduce the machining error of the low stiffness region effectively without influencing the machining error of the non-optimized region.

6.3 The surface quality of the machined blade

Since the radial depth of cut of the optimized cutting path is changed, an evaluation of surface roughness is needed. The measuring equipment is InfiniteFocus G4 made by Alicona. According to the clamping and distribution of the optimized cutting path, the tip and root regions of the blade are chosen for evaluating the surface roughness. Based on the surface roughness evaluation standard, the cut-off length is 0.8 mm, and the scanned images and data figures are shown in Fig. 26. The

Fig. 26 The scanned images and the data figures of a the tip and b root regions of *Path*₃



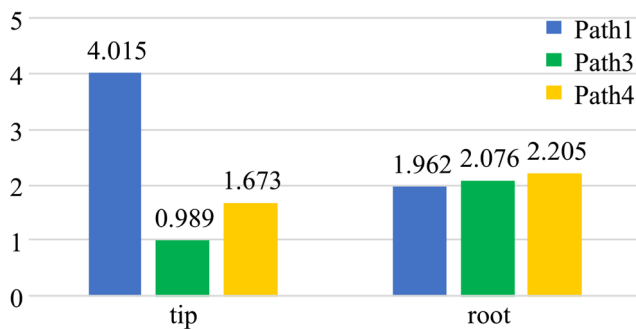


Fig. 27 The surface roughness R_a of root and tip regions (μm)

arithmetic mean deviation, R_a , of the tip and root regions is shown in Fig. 27.

From the measuring results, the R_a values of the root regions of different cutting paths are relatively close due to the constant radial depth of cut. Nevertheless, the R_a of the tip region is increased due to the vibration of the thin-walled part machining [28]. Thanks to the optimization in $Path_3$ and $Path_4$, the decreased radial depth of cut leads to lower R_a values. It should be noticed that the radial depth of cut of the cutting lines in the tip region of $Path_4$ is different and the R_a of this region is larger than that of $Path_3$.

Applying the optimization process, the radial depth of cut and the final surface roughness are changed after blade milling. However, for the milling process, the machining precision should be satisfied first. The surface quality can be improved by the subsequent grinding process.

Integrating the machining time, overall machining errors and the comparison of the local machining errors, the following conclusions can be drawn:

- 1) Comparing the machining times and the machining errors between $Path_1$ and $Path_2$, it could be concluded that the cutting path removing the low stiffness region preferentially can generate a relatively small machining error and should be utilized first.
- 2) Comparing the local machining errors, it could be concluded that the optimized cutting path can excessively reduce the machining error of the low stiffness area, and two optimization algorithms of the radial depth of cut developed in the paper can lead to the similar machining results.
- 3) Comparing the machining times and the overall machining errors of all cutting paths, it could be found that the optimized cutting path can further reduce the machining error and increase the machining time. However, if the same machining accuracy is achieved with the parallel inward cutting path like $Path_1$, the radial depth of cut should be enormously decreased; as a result, the machining time increases exponentially.

Considering the machining time and accuracy comprehensively, the optimization method for the radial depth of cut is effective to improve the machining precision. Especially, the single-point optimization algorithm applied in $Path_4$ is the most effective method of tool path planning method which takes into account the machining efficiency and accuracy.

7 Conclusion

Due to the low stiffness of the thin-walled part, the larger deformation occurs in the milling process and influences the machining precision and quality; furthermore, the final part cannot match the design standard and limit the performance. In this paper, the elastic deformation error model of the thin-walled part milling process is established to optimize the radial depth of cut based on the stable-state deformation field, and the optimized cutting path is generated in milling the thin-walled blade, resulting in a higher machining precision. The key conclusions are summarized as follows:

- 1) For the thin-walled blade milling process, the cutting path milling the low stiffness region preferentially can reach a lower machining deformation error. The average and maximum errors of the vertical inward path are 2.264 and 3.539 times of the parallel inward path, respectively.
- 2) The radial depth of cut optimization method based on the elastic deformation error model of the thin-walled part milling process can reduce the machining deformation error further. Comparing to the non-optimized parallel inward path, the average errors of the optimized parallel inward path and the single-point optimization path are reduced by 23.1 and 26.3%, respectively, and the average errors of the local optimized region are reduced by 53.0 and 60.7%, respectively.
- 3) Considering the machining efficiency and accuracy comprehensively, the single-point optimization algorithm is the most effective optimization method of the radial depth of cut for tool path planning.

Funding The authors gratefully acknowledge the financial support of the National Science and Technology Major Project (Grant No. 2017ZX04011013), Shaanxi Key Research and Development Program in Industrial Domain (Grant No.2018ZDXM-GY-063) and the Fundamental Research Funds for the Central Universities (Grant No.31020200504003).

Compliance with ethical standards

Competing interests The authors declare that they have no competing interest.

References

- Bera TC, Desai KA, Rao PVM (2011) Error compensation in flexible end milling of tubular geometries. *J Mater Process Technol* 211(1):24–34
- Luo M, Han C, Hafeez HM (2019) Four-axis trochoidal toolpath planning for rough milling of aero-engine blisks. *Chin J Aeronaut* 32(8):2009–2016
- Luo M, Yan D, Wu B, Zhang D (2016) Barrel cutter design and toolpath planning for high-efficiency machining of freeform surface. *Int J Adv Manuf Technol* 85(9-12):2495–2503
- Wang J, Ibaraki S, Matsubara A (2017) A cutting sequence optimization algorithm to reduce the workpiece deformation in thin-wall machining. *Precis Eng* 50:506–514
- Budak E, Comak A, Ozturk E (2013) Stability and high performance machining conditions in simultaneous milling. *CIRP Ann Manuf Technol* 62(1):403–406
- Kolluru K, Axinte D, Becker A (2013) A solution for minimising vibrations in milling of thin walled casings by applying dampers to workpiece surface. *CIRP Ann Manuf Technol* 62(1):415–418
- Yang Y, Xie R, Liu Q (2017) Design of a passive damper with tunable stiffness and its application in thin-walled part milling. *Int J Adv Manuf Technol* 89(9):2713–2720
- Ratchev S, Liu S, Huang W, Becker AA (2004) Milling error prediction and compensation in machining of low-rigidity parts. *Int J Mach Tool Manu* 44(15):1629–1641
- Budak E, Altintas Y (1995) Modeling and avoidance of static form errors in peripheral milling of plates. *Int J Mach Tool Manu* 35(3):459–476
- Ratchev S, Nikov S, Moualek I (2004) Material removal simulation of peripheral milling of thin wall low-rigidity structures using FEA. *Adv Eng Softw* 35(8-9):481–491
- Ratchev S, Liu S, Huang W, Becker AA (2006) An advanced FEA based force induced error compensation strategy in milling. *Int J Mach Tool Manu* 46(5):542–551
- Wan M, Zhang W, Qiu K, Gao T, Yang Y (2005) Numerical prediction of static form errors in peripheral milling of thin-walled workpieces with irregular meshes. *J Manuf Sci E* 127(1):13–22
- Kang Y, Wang Z (2013) Two efficient iterative algorithms for error prediction in peripheral milling of thin-walled workpieces considering the in-cutting chip. *Int J Mach Tool Manu* 73:55–61
- Cho MW, Kim GH, Seo TI, Hong YC, Cheng H (2006) Integrated machining error compensation method using OMM data and modified PNN algorithm. *Int J Mach Tool Manu* 46(12-13):1417–1427
- Brandy HT, Donmez MA, Gilsinn DE, Han CS, Kennedy MD (2001) A methodology for compensating errors detected by process-intermittent inspection. US Department of Commerce, NIST
- Guiassa R, Mayer JRR (2011) Predictive compliance based model for compensation in multi-pass milling by on-machine probing. *CIRP Ann Manuf Technol* 60(1):391–394
- Cho MW, Seo TI, Kwon HD (2003) Integrated error compensation method using OMM system for profile milling operation. *J Mater Process Technol* 136(136):88–99
- Hou Y, Zhang D, Mei J, Zhang Y, Luo M (2019) Geometric modeling of thin-walled blade based on compensation method of machining error and design intent. *J Manuf Process* 44:327–336
- Slavkovic NR, Milutinovic DS, Glavonjic MM (2014) A method for off-line compensation of cutting force-induced errors in robotic machining by tool path modification. *Int J Adv Manuf Technol* 70(9):2083–2096
- Tang A, Liu Z (2008) Deformations of thin-walled plate due to static end milling force. *J Mater Process Technol* 206(1–3):345–351
- Yan Q, Luo M, Tang K (2018) Multi-axis variable depth-of-cut machining of thin-walled workpieces based on the workpiece deflection constraint. *Comput Aided Des* 100:14–29
- Feng HY, Li H (2002) Constant scallop-height tool path generation for three-axis sculptured surface machining. *Comput Aided Des* 34(9):647–654
- Chiou CJ, Lee YS (2002) A machining potential field approach to tool path generation for multi-axis sculptured surface machining. *Comput Aided Des* 34(5):357–371
- Hu P, Tang K (2016) Five-axis tool path generation based on machine-dependent potential field. *INT J Comput Integ M* 29(6):636–651
- Koike Y, Matsubara A, Yamaji I (2013) Design method of material removal process for minimizing workpiece displacement at cutting point. *CIRP Ann Manuf Technol* 62(1):419–422
- Lee CM, Kim SW, Choi KH, Lee DW (2003) Evaluation of cutter orientations in high-speed ball end milling of cantilever-shaped thin plate. *J Mater Process Technol* 140(1-3):231–236
- Ko JH, Yun WS, Cho DW, Ehmann KF (2002) Development of a virtual machining system, Part 1: Approximation of the size effect for cutting force prediction. *Int J Mach Tool Manu* 42(15):1595–1605
- Wu TY, Lei KW (2019) Prediction of surface roughness in milling process using vibration signal analysis and artificial neural network. *Int J Adv Manuf Technol* 102:305–314

Publisher's note Springer Nature remains neutral with regard to jurisdictional claims in published maps and institutional affiliations.